Origin of elliptic flow and its dependence on the equation of state in heavy ion reactions at intermediate energies

A. Le Fèvre,[1] Y. Leifels,[1] C. Hartnack,[2] and J. Aichelin[2,3]

[1]*GSI Helmholtzzentrum für Schwerionenforschung GmbH, Planckstrasse 1, 64291 Darmstadt, Germany*
[2]*SUBATECH, IMT Atlantique, Université de Nantes, IN2P3/CNRS 4 rue Alfred Kastler, 44307 Nantes cedex 3, France*
[3]*Frankfurt Institute for Advanced Studies, Ruth Moufang Strasse 1, 60438 Frankfurt, Germany*

Recently it has been discovered that the elliptic flow, v_2, of composite charged particles emitted at midrapidity in heavy-ion collisions at intermediate energies shows the strongest sensitivity to the nuclear equation of state (EoS), which has been observed up to now within a microscopic model. This dependence on the nuclear EoS is predicted by quantum molecular dynamics (QMD) calculations [A. Le Fèvre *et al.*. Nucl. Phys. A **945**, 112 (2016)], which show as well that the absorption or rescattering of in-plane emitted particles by the spectator matter is not the main reason for the EoS dependence of the elliptic flow at midrapidity but different density gradients (and therefore different forces) in the direction of the impact parameter (*x* direction) as compared to the direction perpendicular to the reaction plan (*y* direction), caused by the presence of the spectator matter. The stronger density gradient in the *y* direction accelerates the particles more and creates therefore a negative v_2. When using a soft momentum-dependent EoS, the QMD calculations reproduce the experimental results.

I. INTRODUCTION

The elliptic flow at midrapidity, originally called out-of-plane emission or squeeze-out, has attracted a lot of attention during recent years. It has been predicted in hydrodynamical simulations of heavy ion reactions [1–3] and has later been found experimentally by the Plastic Ball collaboration [4].

The elliptic flow is described by the second moment of the Fourier expansion v_2 of the azimuthal angle ϕ distribution of the emitted particles with respect to the reaction plane Φ_{RP}. All expansion coefficients v_n are typically functions of rapidity $y = \frac{1}{2}\ln(\frac{E+p_z}{E-p_z})$ and of transverse momentum p_t of the particle:

$$\frac{d\sigma(y, p_t)}{d\phi} = C(1 + 2v_1(y, p_t)\cos(\phi - \Phi_{RP})$$
$$+ 2v_2(y, p_t)\cos 2(\phi - \Phi_{RP}) + ...) \quad (1)$$

The Fourier coefficients are then determined by

$$\langle v_n(y, p_t)\rangle = \langle\cos[n(\phi - \Phi_{RP})]\rangle,$$
$$\text{with } v_2 = \frac{p_x^2 - p_y^2}{p_x^2 + p_y^2}, \quad (2)$$

where the angular brackets denote an averaging over all events and particles at y and p_t. A positive v_2 value characterizes a preferred emission in the reaction plane and a negative value an emission out of the reaction plane. In Fig. 1, experimental results of v_2 parameters for $Z = 1$ particles at midrapidity for semicentral Au+Au collisions at various energies are compiled.

At ultrarelativistic energies the measured elliptic flow and its centrality dependence has been considered as an experimental proof that during the expansion of the system the almond shaped initial spatial configuration of the overlap region is transformed into an elliptic flow with a *positive* v_2 value as predicted by hydrodynamics [5]. At lower energies various experimental groups [4,6] and later the FOPI collaboration [7] have investigated the elliptic flow and found a *negative* v_2 coefficient up to beam energies of $\approx 6A$ GeV with a minimum at around $0.4-0.6A$ GeV [8–10]. Therefore, the elliptic flow has to be of different origin at these energies. It has been suggested in Ref. [11] that the v_2 values are negative at low energies because the compressed matter expands while the spectator matter is still present and blocks the in-plane emission. At higher incident energies the expansion takes place after the spectator matter has passed the compressed zone and therefore the elliptic flow is determined by the shape of the overlap region only, which leads to a positive v_2. The negative v_2 at low incident energies is due to shadowing overlaid by an expansion of the compressed overlap zone [9]. The minimum of the elliptic flow v_2 coincides with the maximum of nuclear stopping at these energies [12] and high baryon densities are reached during the collision. Contrary to findings at higher beam energies where fluctuations contribute to the elliptic flow (see, e.g., Refs. [13,14]) there is no convincing experimental evidence at beam energies between $0.4A$ and $2A$ GeV that event-by-event fluctuations play a significant role in the elliptic flow pattern [15]. The interactions with the surrounding spectator matter and the much longer collision times might be responsible for this. At even lower incident energies v_2 becomes positive again, because the attractive NN forces outweigh the repulsive NN collisions. This phenomenon has been discussed in various publications, e.g., Refs. [16–18].

Recently, the FOPI collaboration has compared its experimental findings on elliptic flow v_2 of light charged particles
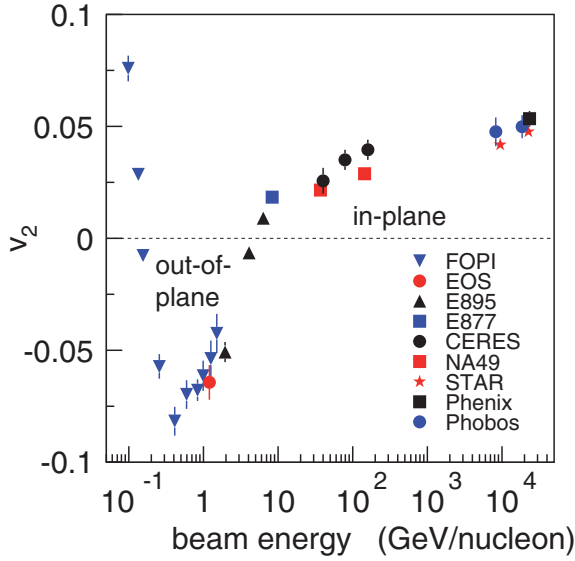
FIG. 1. Elliptic flow v_2 of $Z = 1$ particles at midrapidity as a function of incident beam energy in semicentral ^{197}Au $+ ^{197}$Au collisions as measured by various experiments, indicated by the different symbols. Data are extracted from Refs. [6,8,10,11].

measured in Au+Au collisions with results obtained in the framework of quantum molecular dynamics (QMD) calculations [19]. One conclusion was that the elliptic flow at energies between $0.2A$ and $2.0A$ GeV has the largest dependence on the stiffness of the nuclear EoS of all observables studied so far, an even larger dependence than found earlier in Kaon production [20]. These findings created therefore a renewed interest to study in detail the origin of the elliptic flow and its dependence on the EoS. In this article we report on investigations using the isospin QMD model. In Sec. II we will shortly introduce the QMD approach, which we use for the analysis. Section III is devoted to a survey of the reaction, especially to a comparison of the reaction scenarios for different EoSs. In Sec. IV we study in detail the elliptic flow created in these reaction and analyze its origin and its EoS dependence. We summarize our work in Sec. V.

II. THE QUANTUM MOLECULAR DYNAMICS APPROACH

The details of the QMD approach have been published in Refs. [21–23]. Comparisons to experimental benchmark data measured in the incident energy region under consideration are published in Ref. [7]. Here, we quote only how this approach allows for an exploration of the nuclear EoS:

Nucleons are represented as Gaussian wave functions. A generalized Ritz variational principle allows to determine the time evolution of the centroids of the Gaussians in coordinate r_i and momentum space p_i,

$$\dot{r}_i = \frac{\partial \langle H \rangle}{\partial p_i} \quad \dot{p}_i = -\frac{\partial \langle H \rangle}{\partial r_i}, \tag{3}$$

TABLE I. Parameter sets for the nuclear equation of state used in the IQMD model.

	α (MeV)	β (MeV)	γ	δ (MeV)	ε ($\frac{c^2}{\text{GeV}^2}$)	K (MeV)
SM	-390	320	1.14	1.57	500	200
HM	-130	59	2.09	1.57	500	376

where the expectation value of the total Hamiltonian H is

$$\langle H \rangle = \langle T \rangle + \langle V \rangle$$
$$= \sum_i \frac{p_i^2}{2m_i} + \sum_i \sum_{j>i} \int f_i(\mathbf{r},\mathbf{p},t) V(\mathbf{r},\mathbf{r}',\mathbf{p},\mathbf{p}')$$
$$\cdot f_j(\mathbf{r}',\mathbf{p}',t) \, d\mathbf{r} \, d\mathbf{r}' d\mathbf{p} \, d\mathbf{p}'. \tag{4}$$

f_i is the single-particle Wigner density

$$f_i(\mathbf{r},\mathbf{p},t) = \frac{1}{\pi^3 \hbar^3} e^{-\frac{2}{L}(\mathbf{r}-\mathbf{r_i}(t))^2} e^{-\frac{L}{2\hbar^2}(\mathbf{p}-\mathbf{p_i}(t))^2}. \tag{5}$$

The potential consists of several terms:

$$V(\mathbf{r_i},\mathbf{r_j},\mathbf{p_i},\mathbf{p_j}) = G + V_{\text{Coul}}$$
$$= V_{\text{Skyrme}} + V_{\text{Yuk}} + V_{\text{mdi}} + + V_{\text{sym}} + V_{\text{Coul}}$$
$$= t_1 \delta(\mathbf{r_i} - \mathbf{r_j}) + t_2 \delta(\mathbf{r_i} - \mathbf{r_j}) \rho^{\gamma-1}(\mathbf{r_i})$$
$$+ t_3 \frac{\exp\{-|\mathbf{r_i} - \mathbf{r_j}|/\mu\}}{|\mathbf{r_i} - \mathbf{r_j}|/\mu}$$
$$+ t_4 \ln^2(1 + t_5(\mathbf{p_i} - \mathbf{p_j})^2) \delta(\mathbf{r_i} - \mathbf{r_j})$$
$$+ t_6 \frac{1}{\varrho_0} T_3^i T_3^j \delta(\mathbf{r_i} - \mathbf{r_j}) + \frac{Z_i Z_j e^2}{|\mathbf{r_i} - \mathbf{r_j}|}. \tag{6}$$

The total one-body Wigner density is the sum of the Wigner densities of all nucleons. The nuclear EoS, however, describes the properties of infinite nuclear matter (without Coulomb interactions) and is therefore given by the volume energy only. The EoS describes the variation of the energy $E(T = 0, \rho/\rho_0)$ when changing the nuclear density to values different from the saturation density ρ_0 for zero temperature.

The single-particle potential resulting from the convolution of the distribution functions f_i and f_j with the interactions $V_{\text{Skyrme}} + V_{\text{mdi}}$ (local interactions including their momentum dependence) is for symmetric nuclear matter

$$U_i(\mathbf{r_i},t) = \alpha \left(\frac{\rho_{\text{int}}}{\rho_0}\right) + \beta \left(\frac{\rho_{\text{int}}}{\rho_0}\right)^\gamma$$
$$+ \delta \ln^2(\varepsilon(\Delta \mathbf{p})^2 + 1) \left(\frac{\rho_{\text{int}}}{\rho_0}\right), \tag{7}$$

where ρ_{int} is the interaction density obtained by convoluting the distribution function of a particle with the distribution functions of all other particles of the surrounding medium. $\Delta \mathbf{p}$ is the relative momentum of a particle with respect to the surrounding medium.

In nuclear matter the parameters t_1, t_2, t_4, t_5 in Eq. (7) are uniquely related to the coefficients α, β, δ, and ϵ in Eq. (7). Values of these parameters for the different model choices can be found in Table I.

The parameters ϵ and δ are given by fits to the optical potential extracted from elastic scattering data in pA collisions [24,25]. Two of the three remaining parameters of the ansatz are fixed by the condition that the volume energy has a minimum of $E/A(\rho_0) = -16$ MeV at ρ_0.

The third parameter is historically expressed as the compression modulus K of nuclear matter, which corresponds to the curvature of the volume energy at $\rho = \rho_0$ (for $T = 0$) and is also given in Table I

$$ K = -V\frac{\partial p}{\partial V} = 9\rho^2 \frac{\partial^2 E/A(\rho)}{(\partial\rho)^2}|_{\rho=\rho_0}. \quad (8) $$

An equation of state with a rather low value of the compression modulus K yields a weak repulsion of compressed nuclear matter and thus describes "soft" matter (denoted by "SM"). A high value of K causes a strong repulsion of nuclear matter under compression (called a "hard EoS," HM).

Generally, there is a good agreement between the model results and experimental data. Critical input parameters, like cross sections, are confined by experimental observations. Shortcomings of the model are pion production and the formation of heavy clusters at midrapidity, which are discussed in detail in Ref. [19].

III. SURVEY OF THE REACTION

Motivated by the good agreement between experimental data and the results of the IQMD model in most of the relevant flow observables [7,19], we use this model to understand the reaction in its full complexity. ^{197}Au + ^{197}Au collisions at $0.6A$ and $1.5A$ GeV and an impact parameter of 6 fm are used as model cases, because at around $0.6A$ GeV the elliptic flow excitation function reaches its minimum and $1.5A$ GeV is the highest energy measured by the FOPI collaboration. For the following discussion, only protons were taken into consideration. We verified that neither the formation of clusters nor the behavior of neutrons alter our findings.

The time evolution of the heavy ion reaction ^{197}Au + ^{197}Au at $E_{kin} = 1.5A$ GeV and an impact parameter $b = 6$ fm is shown in Fig. 2. The density profile of protons, ($\rho_{ij} = \frac{1}{N_{event}}\int\frac{dN_p}{didjdk}dk$, where i,j,k represent the three space coordinates x,y,z) at different times expressed in units of the passing time t_{pass} is presented. The passing time, t_{pass}, is the time the nuclei need to pass each other completely assuming that they do not experience deceleration and therefore continue moving with their initial velocity. For ^{197}Au + ^{197}Au collisions at $E_{kin} = 0.6A$ GeV the passing time is $t_{pass} = 22.9$ fm/c and 16.9 fm/c for $E_{kin} = 1.5A$ GeV. After t_{pass} the spectator matter (those nucleons of projectile and target which are outside of the overlap of projectile and target) cannot absorb nucleons from the participant region (the nucleons of the overlap region of projectile and target) anymore. Projections of proton densities $\rho(x,y,z)$ onto the zx plane (where x is the direction of the impact parameter and z the direction of the beam), onto the zy plane and onto the xy plane are shown from top to bottom and for three different times $t = 0.1, 0.5, 1.0t_{pass}$ from right to left. As can be seen in the top figures, the central (participant) matter is highly compressed when the overlap of the colliding system is largest at $t = 0.5t_{pass}$. Projectile and target remnants separate
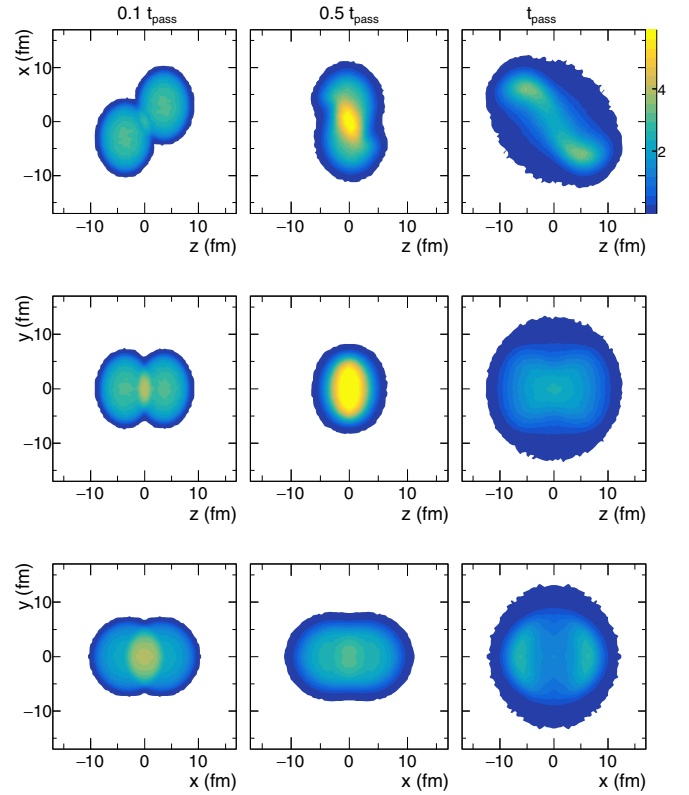

FIG. 2. Time evolution of the proton density profile (ρ_{ij} in event^{-1}fm^{-2}) in the reaction ^{197}Au + ^{197}Au at $1.5A$ GeV incident energy with an impact parameter $b = 6$ fm. A SM EoS is applied in the calculations. Different projections are shown: projections onto the zx plane in the top row, onto the zy plane in the middle, and onto the xy plane in the bottom. The density profile are shown at different times: 2, 8, and 16 fm/c (0.1, 0.5, 1.0 t_{pass}) in the left, central and right columns, respectively.

but they are connected for longer than t_{pass} by a ridge with a quite high particle density. This ridge will disintegrate when projectile and target remnants separate further. The importance of this ridge can be seen in the second row which shows the density profile in the zy plane. In this projection, at half t_{pass}, we observe the highest density at $z = 0$ and therefore in the ridge.

The choice of the EoS influences the reaction scenario predicted by the model. This can be studied in detail by evaluating the difference (SM-HM) of the proton densities projected onto the xy plane, $\Delta\rho_{xy} = \rho_{xy}^{SM} - \rho_{xy}^{HM}$, and correspondingly onto the zx and zy planes. The results are shown in Figs. 3 and 4 in coordinate and velocity space, respectively. The red color signals regions in which a soft EoS yields a higher density, whereas the blue color marks the regions in which the density is higher for a hard EoS. In addition, the positive values are emphasized with black contour lines. Figure 3 (4) displays this density difference at t_{pass} in coordinate (velocity) space for the reaction ^{197}Au + ^{197}Au at $0.6A$ GeV (left) and at $1.5A$ GeV (right). The density of protons in the geometrical overlap region of projectile and target is substantially higher for a soft EoS, as can be seen in the uppermost panels of Fig. 3, whereas at larger distances from the reaction center we observe a higher
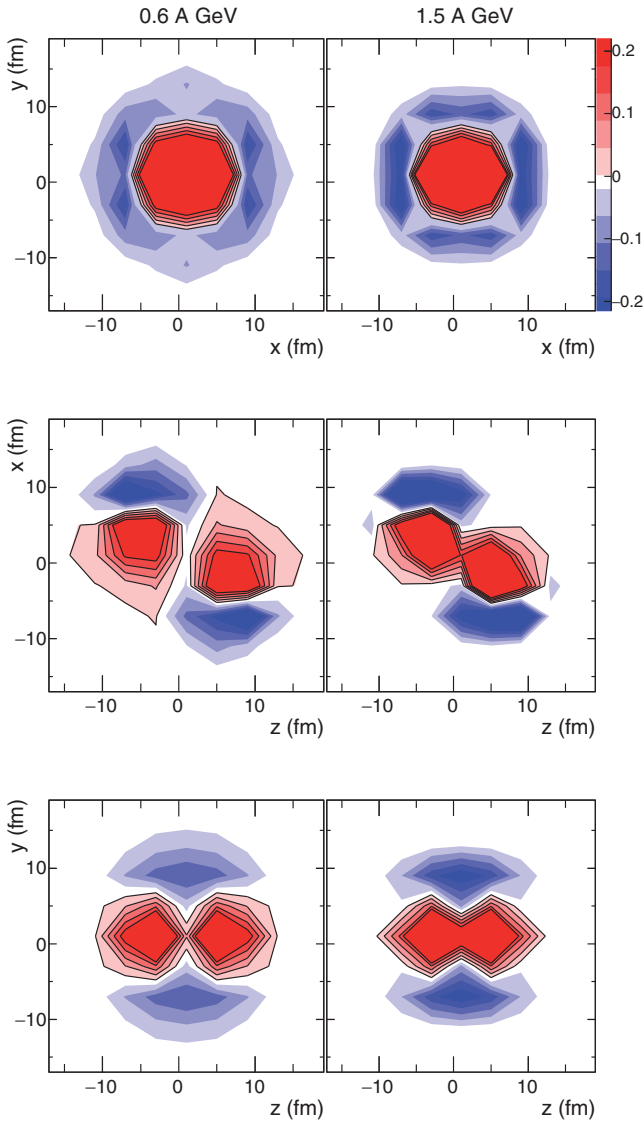
FIG. 3. Difference of the proton density profiles, $\delta\rho_{x,y} = \rho_{xy}{}^{\mathrm{SM}} - \rho_{xy}{}^{\mathrm{HM}}$ in event^{-1}fm^{-2}) between a SM and a HM EoS in the (from top to bottom) xy, zx, and zy planes. Predictions for ^{197}Au $+$ ^{197}Au at 0.6A and 1.5A GeV incident energies are shown on the left and columns, respectively. The impact parameter is 6 fm and the model results are for $t = t_{\mathrm{pass}}$. The red color stands for positive values, the blue color for negative ones. Positive values are emphasized with black contour lines in addition.

density for a hard EoS. At 0.6A GeV this surplus in the density for a hard EoS in the xy plane is larger in the x direction, but it becomes rather isotropic at 1.5A GeV. The origin of this surplus in the x direction is rather different from that in the y direction: in the middle panel of Fig. 3 is shown that the excess in the x direction has its origin in the in-plane flow of the spectator matter expressed by a finite v_1 coefficient in Eq. (1). This in-plane flow is considerably stronger for a hard EoS as compared to a soft one [25–27]. In the y direction the surplus in density of the hard EoS is concentrated at around $z = 0$, being less extended but stronger at higher energies (Fig. 3 lower panels). The emission of these particles is caused by a stronger
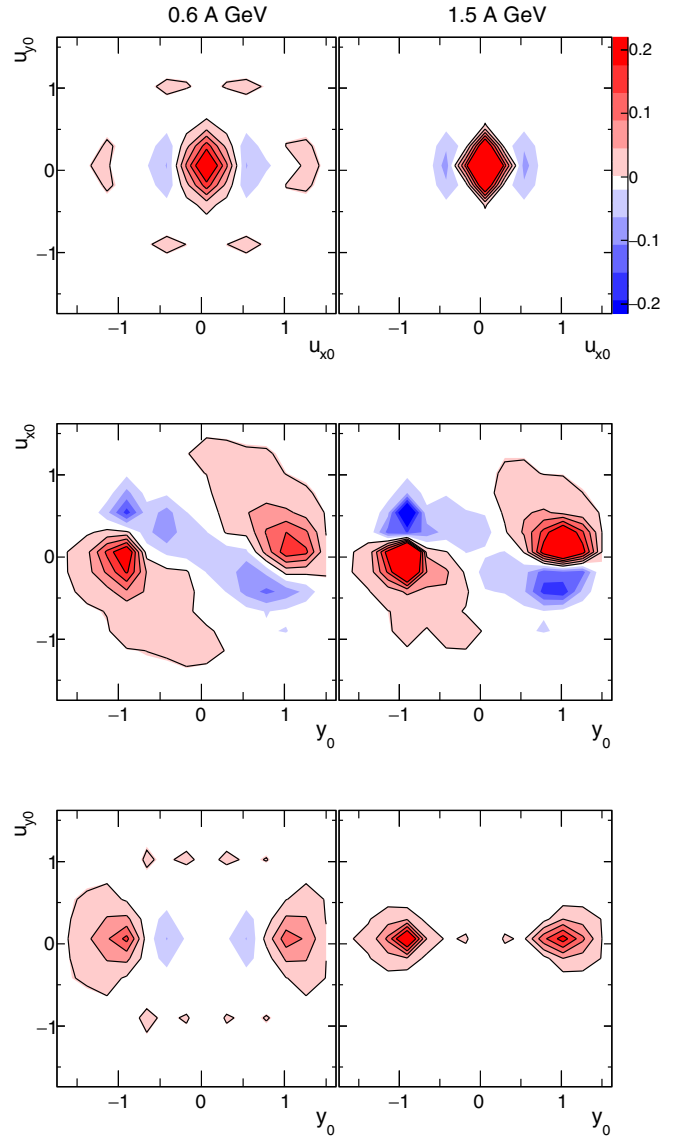
FIG. 4. Same as Fig. 3 but expressed in the planes of (u_{x0}, u_{y0}), (u_{x0}, y_0), (u_{y0}, y_0) scaled velocities (see text).

density gradient (and hence a stronger force) in y direction for a HM EoS as compared to a SM one.

To analyze the model results in momentum space we introduce the transverse vector $\frac{\vec{p}_t}{m} = \vec{u}_t = \vec{\beta}_t \gamma_t$ with $\vec{\beta}_t = (\beta_x, \beta_y)$. The three-vector $\vec{\beta}$ is the velocity in units of the light velocity and $\gamma = 1/\sqrt{1 - \beta^2}$. Throughout, we use scaled units for the rapidity $y_0 = y/y_p$ and the transverse velocity $\vec{u}_{t0} = (u_{x0}, u_{y0}) = \vec{u}_t/u_p$, with $u_p = \beta_p \gamma_p$, the index p referring to the incident projectile in the center of the colliding system. In these units the initial target-projectile rapidity gap always extends from $y_0 = -1$ to $y_0 = 1$.

In velocity space (Fig. 4) we observe a complementary distribution. In the xy plane (upper panels) the shift of protons in the x direction is smaller for a SM than for a HM EoS due to a smaller acceleration yielding a weaker in-plane flow and hence a smaller velocity in the x direction (see middle panels).
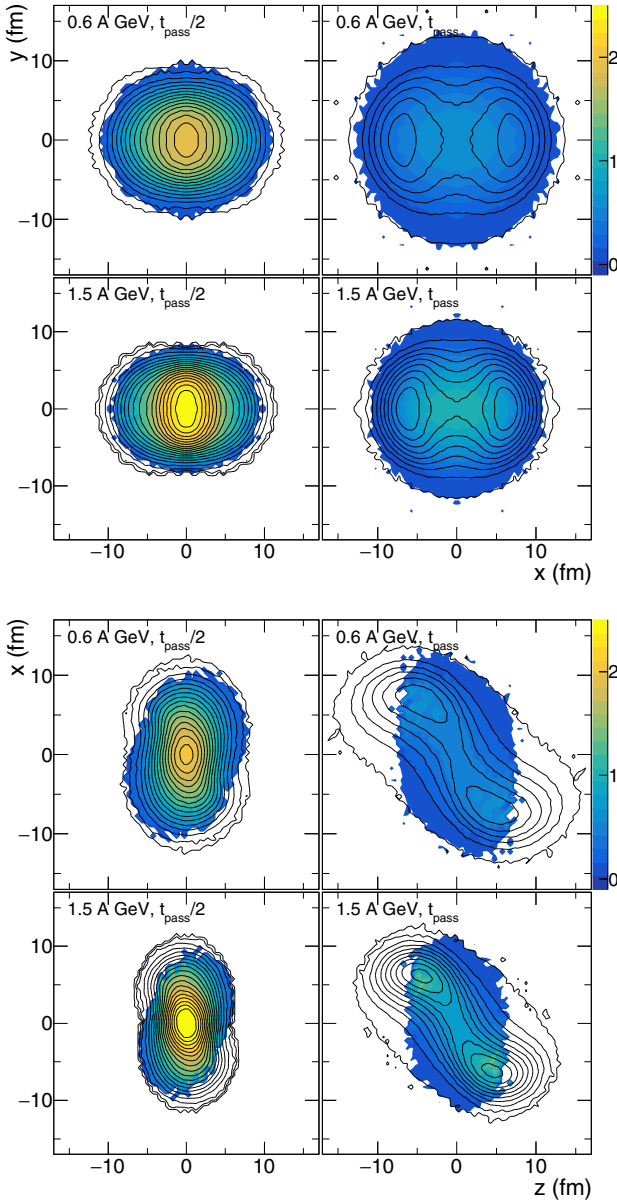
FIG. 5. Mean reduced baryonic density (ρ/ρ_0) in coordinate space as perceived by protons in ^{197}Au $+$ ^{197}Au collisions with a SM EoS, $b = 6$ fm, at 0.6A (top) and 1.5A (bottom) GeV incident energies, at two different times: at full overlap of the system $0.5t_{\text{pass}}$ (left) and at the passing time t_{pass} (right). Black lines and colored contours correspond to all protons and to those finally emitted at midrapidity ($|y_0| < 0.2$) with a high transverse velocity ($u_{t0} > 0.4$), respectively. The top four-panel groups show projections on xy plane, and the lower ones show projections on the xz planes.

The soft EoS leads also to less stopping, as can be seen in the lower panels.

Fast moving particles in the transverse direction at midrapidity are selected by applying the following cuts: $|y_0| < 0.2$, $u_{t0} > 0.4$. Identical cuts were used by the FOPI collaboration for the investigation of elliptic flow. Figure 5 shows the averaged normalized nuclear density (ρ/ρ_0) obtained for a SM EoS for this selection of participant protons in the xy

plane (upper four panels) and in the zx plane (lower four panels) for 0.6A and 1.5A GeV incident energies at $t = 0.5t_{\text{pass}}$ (left column) and $t = t_{\text{pass}}$ (right column). The density profiles are integrated over the third dimension. We confront this average density (color scaled) of protons finally observed with high velocities at midrapidity with the density of all protons (contours). We observe that at full overlap, $t = 0.5t_{\text{pass}}$, the innermost participants form a dense almond shaped core which is out-of-plane elongated. This is the target-projectile overlap region, where the compression is highest. On the contrary, the outermost participants, which form a more dilute medium, are extending in-plane, aligned with the spectator distribution, though slightly tilted as a consequence of stopping. Later, at passing time (right panel), the innermost (compressed) participants expand in-plane, but not with enough pressure to produce a positive elliptic flow v_2, as we will see later. This is in contrast to the situation at higher bombarding energies where the strength of the compression is high enough to make the in-plane expansion dominant. The outermost participants undergo a twofold evolution: First by expanding out-of-plane (seen on the xy plane) which will produce a negative v_2 as will be shown later. Second by forming an in-plane ridge between the bulk of the spectators (seen on the xz plane). The higher the incident energy the higher is the density of this ridge and of the initial almond shaped core.

IV. THE ELLIPTIC FLOW

Figure 6 shows the time evolution of the elliptic flow $v_2(t) = \frac{p_x^2(t) - p_y^2(t)}{p_x^2(t) + p_y^2(t)}$ of midrapidity protons in the ^{197}Au $+$ ^{197}Au collisions at 0.6A (top) and 1.5A (bottom) GeV for SM (black) and HM (red) nuclear equation of state. The elliptic flow v_2 starts to develop after approximately half the passing time t_{pass} and evolves rapidly. After twice the passing time, v_2 reaches its final value. It is negative for most of the collision times and for both energies. But there is a tendency to be positive in the early stage of the collision. If one selects protons emerging with a high transverse velocity $u_{t0} > 0.4$ (dashed lines) the amplitude of the elliptic flow signal is enhanced and it is mostly negative throughout the whole collision process. Comparing the predictions for a SM and a HM equation of state one notes that the value of v_2 at midrapidity depends strongly on the EoS; this effect is enhanced if protons with a high transverse velocity are selected.

Scattering of nucleons and the mean field (potential) interactions are contributing to the elliptic flow signal. In the simulations, it is possible to distinguish both contributions and investigate how they develop as a function of time. This is achieved by recording the momenta of protons before and after each collision and before and after each time step during which the proton propagates in the potential created by all other nucleons.

Hence, the momentum change due to collisions can be written as

$$\Delta \boldsymbol{P}^{\text{coll}}(t) = \boldsymbol{p}^{\text{coll}}(t) - \boldsymbol{p}(0)$$
$$= \sum_{i=1}^{N_c(t)} \Delta \boldsymbol{p}_i^{\text{coll}}, \qquad (9)$$
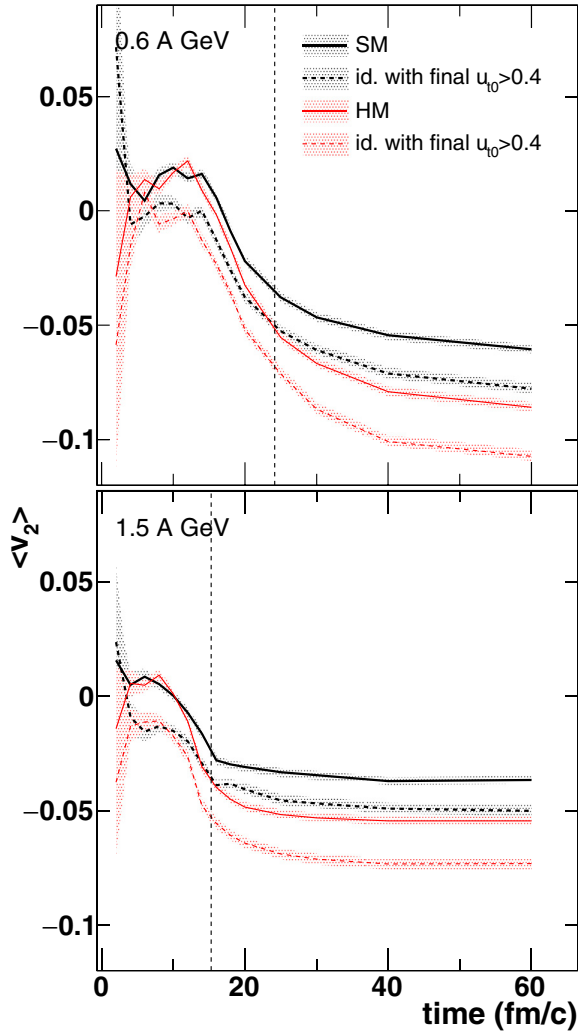
FIG. 6. Time evolution of the average elliptic flow $v_2(t)$ of protons at midrapidity in the ^{197}Au + ^{197}Au collisions at 0.6A (top) and 1.5A (bottom) GeV incident energies, $b = 6$ fm. We show results obtained with a HM (red lines) and a SM (black lines) EoS, and with (dashed lines) or without (full lines) excluding the protons having finally a low transverse velocity $u_{t0} \leqslant 0.4$. The dashed vertical lines indicate the passing time, and the grayed areas the statistical uncertainties.

where $N_c(t)$ is the number of collisions a particle experiences until time t, Δp_i^{coll} is the momentum transfer in the ith collision, and $p(0)$ is the initial momentum of the particle.

For potential interactions the time-integrated momentum change is

$$\Delta P^{\text{m.f.}}(t) = p^{\text{m.f.}}(t) - p(0)$$
$$= \sum_{i=0}^{i(t)} \int_{t_i}^{t_{i+1}} \dot{p}^{\text{m.f.}} dt. \qquad (10)$$

With these prescriptions we define the momentum change into the transverse direction as follows:

$$\Delta P_t^{\text{coll,m.f.}}(t) = \left[\Delta P_x^{\text{coll,m.f.}}(t), \Delta P_y^{\text{coll,m.f.}}(t) \right]. \qquad (11)$$
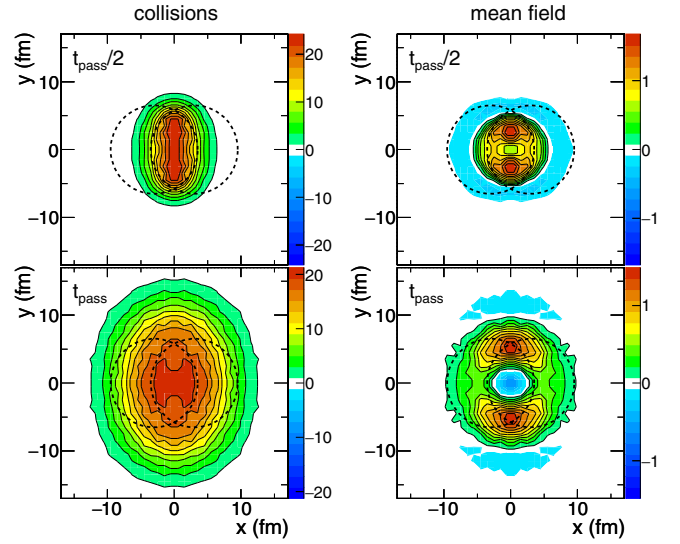

FIG. 7. IQMD (with SM EoS) predictions for midcentral ($b = 6$ fm) collisions of ^{197}Au + ^{197}Au at 0.6A GeV incident energy, at two times: $t_{\text{pass}}/2$ (maximal overlap) and t_{pass}, top and bottom panels respectively. The panels display $\Delta P_t^o(t)$ in MeV/fm^2/event defined in the text as a function of the (x, y) positions of protons at the respective times. Only protons finally at midrapidity ($|y_0| < 0.2$) are selected. The left and right panels show the momentum transfer due to collisions and to the mean field, respectively. As a reference, the superimposed circles show the spatial extension of the incoming projectile and target in this plane. Positive values are marked by black contour lines.

To visualize the effect of the momentum transfers on the elliptic flow phenomena more strongly, we project the transverse momentum transfer vector onto the final momentum vector of the particle p_{final}

$$\langle \Delta P_t^o(t) \rangle = \left\langle \Delta P_t(t) \cdot \frac{p_{\text{final}}}{|p_{\text{final}}|} \right\rangle. \qquad (12)$$

The angular brackets denote an averaging over events and particles.

Figures 7 and 8 show this *oriented* transverse momentum change $\langle \Delta P_t^o(t) \rangle$ for beam energies of 0.6A and 1.5A GeV, respectively, separately for transverse momentum changes due to collisions (left panel) and due to potential interactions (right panel) at different collision times. The positive values are highlighted by black contour lines. $\langle \Delta P_t^o(t) \rangle$ of protons is shown as a function of their $(x(t), y(t))$ position at half passing time $t = t_{\text{pass}}/2$ (top) and at passing time $t = t_{\text{pass}}$ (bottom). Protons are selected which are finally emitted at midrapidity ($|y_0| < 0.2$). Comparing the scales of the left and right panels, one first observes that the transverse momentum transfer due to collisions is about an order of magnitude larger than that due to potentials.

In the overlap zone of projectile and target, where the number of collisions is highest, the collisions create quite early (at half passing time) a large value of $\langle \Delta P_t^o(t) \rangle$. This means that the momentum transfer is large in the initial violent collisions and the direction of the particle momentum is—on the average—already close to the final one. Because the nucleons gained a considerable transverse momentum, this
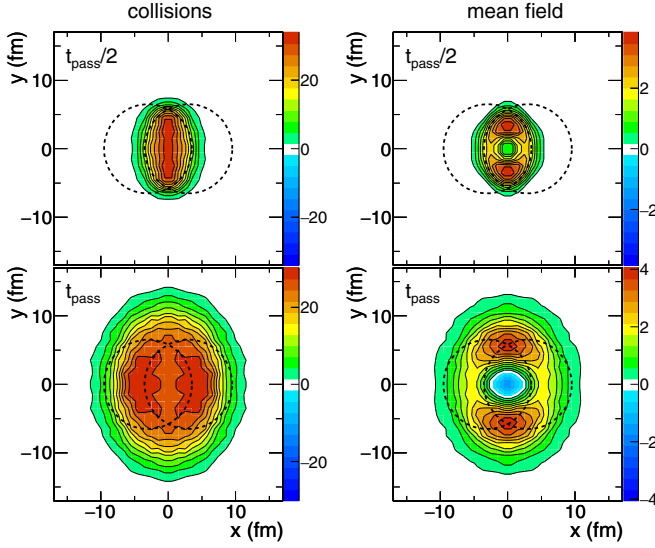
FIG. 8. Same as described in the caption of Fig. 7 for 1.5A GeV incident energy.

zone of violent collisions expands rapidly keeping its almond shape.

$\langle \Delta P_t^o(t) \rangle$ due to potential interactions shows a quite different structure. The out-of-plane momentum transfer is large in the vicinity of the tips of the almond shape overlap zone because these nucleons are directly situated between vacuum and the central densest zone. Therefore, they feel the highest density gradient and hence the largest force. The comparison of the top (half passing time) and bottom rows (passing time) shows how these accelerated particles move in y direction out of the overlap zone. Qualitatively there is little difference between the reaction at 0.6A GeV and at 1.5A GeV. Particles distant from the center of the reaction show a negative $\langle \Delta P_t^o(t) \rangle$. They are feeling the attractive potential of the remnant and are getting decelerated. There is also a zone around the origin where $\langle \Delta P_t^o(t) \rangle$ is negative. As Fig. 2 top right shows, these nucleons form the ridge between projectile and target remnant. The density of the ridge around $z = x = y = 0$ decreases between $t_{\text{pass}}/2$ and t_{pass}. But the nuclear matter is attracted by the moving spectators in the xz plane and its velocity in transverse direction is reduced.

The elliptic flow v_2 is not related to the magnitude of the transverse momentum change $\langle \Delta P^o(t) \rangle$ but to its anisotropy in x and y. To access this situation the quantity $\Delta P_{y-x}^o(t) = \Delta P_y^o(t) - \Delta P_x^o(t)$ is introduced. For a single proton the directed momentum change $\Delta P_i^o(t)$ is defined by the momentum change in x or y direction $\Delta P_i(t)$ projected onto the direction of the respective component of the final momentum vector,

$$\langle \Delta P_i^o(t) \rangle = \left\langle \Delta P_i(t) \cdot \frac{p_{i,\text{final}}}{|p_{i,\text{final}}|} \right\rangle. \quad (13)$$

$\langle \Delta P_i^o \rangle$ is calculated for momentum changes due to potentials and due to collisions defined in Eqs. (10) and (9), respectively.

The resulting quantities are presented in Fig. 9, where results of model calculations are shown for protons emitted at midrapidity, $|y_0| < 0.2$, in ^{197}Au + ^{197}Au collisions of 0.6A
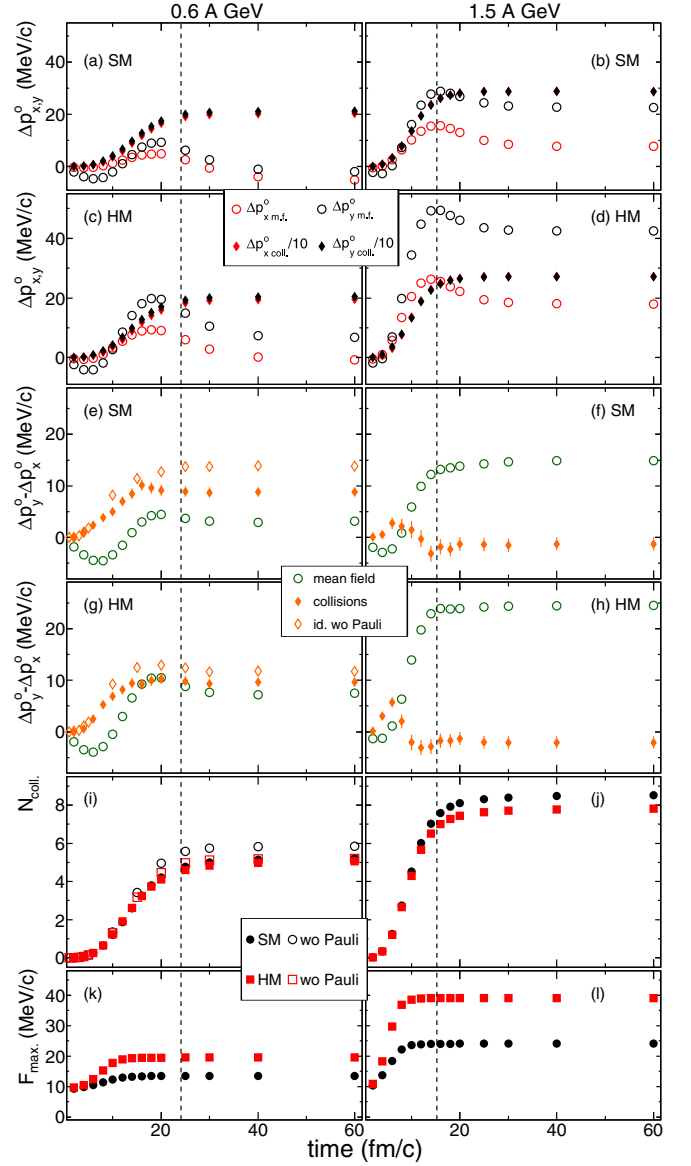

FIG. 9. IQMD predictions of the time evolution of various observables. Protons are selected which are finally observed at midrapidity ($|y_0| < 0.2$) in the midperipheral ($b = 6$ fm) collisions of ^{197}Au + ^{197}Au . Left and right panels show results at 0.6A and 1.5A GeV incident energies, respectively. Panels (a) and (b) show for the SM EoS the integrated momentum transfer in x (red symbols) and y (black symbols) directions, caused by the mean field (m.f., open circles) and by collisions (coll., diamonds). The momentum transfer due to collisions is divided by a factor of 10. Panels (c) and (d): *idem* for the HM EoS. Panels (e) and (f) show for the SM EoS the integrated difference between the out-of-plane (y) and in-plane (x) contribution of the momentum transfer from the mean field (green open circles) and from the collisions with (orange full diamonds) or without (orange empty diamonds) Pauli blocking. Panels (g) and (h): *idem* for the HM EoS. Panels (i) and (j) show the number of collisions suffered by the selected protons comparing the SM (black circles) and HM (red squares) EoSs, with (full symbols) or without (open symbols) Pauli blocking. Panels (k) and (l): *idem* with the maximal force due to the mean field. The vertical dashed lines indicate the passing time.

(right panels) and 1.5A GeV (left panels) at impact parameter $b = 6$ fm. Figures 9(a)–9(d) show the time dependence of the momentum change $\Delta P_x^o(t)$ and $\Delta P_y^o(t)$ integrated up to time t due to mean field interactions (black symbols) and due to collisions (red symbols) for different nuclear equations of state. The integrated momentum change due to collisions is always much larger than the one generated by the mean field. Note, that in this figure the data for momentum changes due to collisions are divided by a factor of 10. For this type of momentum changes one observes only a rather small excess in the y direction (out-of-plane) at the low energy and essentially none at the high energy. But an excess in the y direction is always visible for the momentum changes due to potential interactions. This is quantified in Figs. 9(e)–9(h) where the difference $\Delta P_y^o(t) - \Delta P_x^o(t)$ is presented as a function of time. The excess in the y direction is clearly visible for the potential interaction, but also the collisions produce such an effect with an amplitude which becomes smaller with higher projectile velocity until it vanishes at 1.5A GeV incident energy.

The stiffness of the equation of state has no visible influence on the amplitude of the collisional out-of-plane momentum excess. This is related to the fact that the number of collisions, as displayed in Figs. 9(i) and 9(j), is almost unchanged by the choice of the equation of state. The correlation of the time evolution of the collisional $\Delta P_y^o - \Delta P_x^o$ with the number of collisions is particularly marked at the lower incident energy [Fig. 9(i)].

An additional reason for the EoS independence of the collisional out-of-plane flow is the Pauli blocking. Its influence is only studied for the lower energy because it is negligible at the higher one. The open red diamonds in Figs. 9(e) and 9(g) show the effect on collisional $\Delta P_y^o - \Delta P_x^o$ when switching off Pauli blocking. Without Pauli blocking there is a visible sensitivity to the nuclear EoS for this observables when only collisional contributions are considered. However, Pauli blocking quenches the out-of-plane flow due to collisions, starting from the densest phase of the collisions, at half t_{pass} (maximal overlap). The quenching is stronger for the softer (SM) EoS because the central hadron densities reached during the collision process are larger. Thus, the model predicts that without Pauli blocking there would be a collisional contribution to the EoS dependence of v_2, but with Pauli blocking this sensitivity is vanishing, which finally leads to the observation that there is no collisional contribution to the EoS dependence of the v_2 signal.

The mean field contribution to the out-of-plane momentum flow is enhanced by both, the incident energy and the stiffness of the equation of state: moderate at 0.6A GeV with the SM EoS, contributing to only 30% of the total $\Delta P_y^o - \Delta P_x^o$, very strong and dominating at 1.5A GeV with the HM EoS. This is directly correlated with the strength of the mean field, displayed in Figs. 9(k) and 9(l), nearly doubled for the HM EoS. In conclusion, we observe that the only essential dependence of the out-of-plane flow on the EoS comes from the mean field.

The origin of v_2 is further investigated by analyzing the elliptic flow in the xy plane as a function of the transversal distance of the protons from the center of the reaction. The positions of the protons are evaluated at t_{pass}. The results of such an analysis are presented in Fig. 10. As before, protons were selected which are finally emerging in the midrapidity
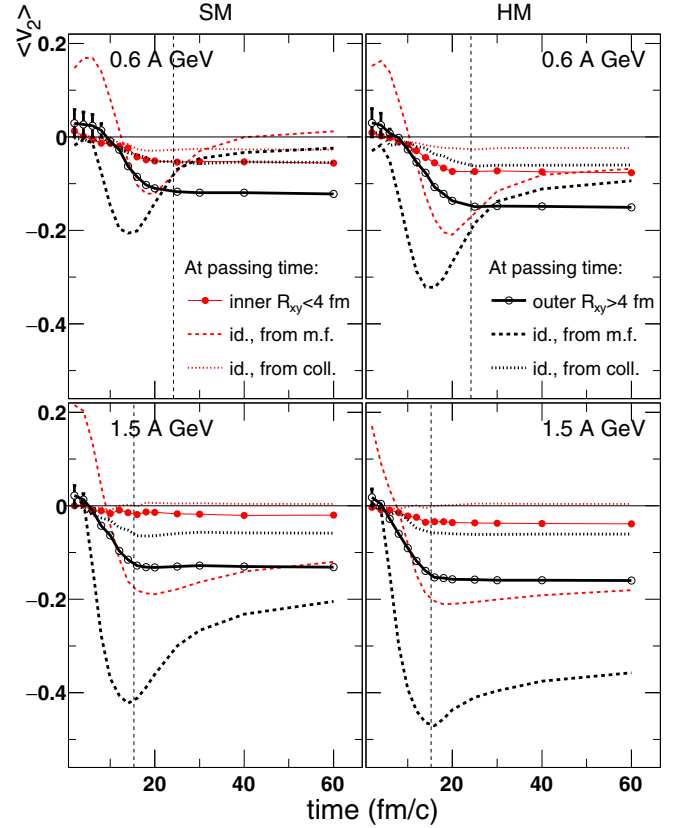

FIG. 10. Time evolution of the average elliptic flow, v_2, of protons finally emitted at midrapidity ($|y_0| < 0.2$) with a large transverse velocity $u_{t0} > 0.4$ in ^{197}Au + ^{197}Au collisions at $b = 6$ fm and at 0.6A (top) and 1.5A (bottom) GeV incident energy, with a SM (right) and a HM (left) EoS. The protons situated, at the passing time, transversally close (radial distance to the center of the collision on the transversal plane $R_{xy} < 4$ fm) or far ($R_{xy} > 4$ fm) to/from the main axis of the collision are distinguished, respectively, by red and black lines. The overall v_2 (symbols) is detailed into its two contributions: the v_2 developed by the momentum transfer due to the mean field and due to the collisions are depicted by dashed and dotted lines, respectively. Black vertical dashed lines indicate the passing time.

region $|y_0| < 0.2$ with high transverse velocity u_{t0}, which only enhances the amplitude of the observed phenomena, as discussed in Fig. 6. First we observe that the collisional contribution to v_2 reaches its asymptotic value early, before or close to the passing time t_{pass}, when collisions cease, as seen in Figs. 9(i) and 9(j). The collisional contribution to v_2 is a fast process because it needs the presence of the spectators to induce an in-plane quenching effect. The mean-field contribution stabilizes at a slightly later time at 0.6A GeV and even later at 1.5A GeV, long after the strength of the force, shown in Figs. 9(k) and 9(l), reaches its maximal value.

Another feature is that the outermost nucleons ($R_{xy} > 4$ fm) are the main source of the overall negative v_2, they develop a much stronger out-of-plane flow. This is observed for the collisional contribution because the early in-plane screening by the spectators affects only the outermost nucleons, whereas the collisions of the inner nucleons create a nearly azimuthally isotropic distribution. We have already seen in Figs. 7 that the

mean field contribution to the negative v_2 originates mostly from the nucleons of the outer region. This is well quantified in Fig. 10. The density gradient is higher in the vicinity of the tips of the overlapping zone of the colliding system. This creates a stronger force and hence a higher momentum flow. The out-of-plane flow, created by the mean field, has reached a maximum at half the passing time for the reaction at the lower energy, $0.6A$ GeV, and at passing time for the higher energy. Later it decreases due to the formation of the in-plane ridge seen in Fig. 5 and due to the mean field which lowers the momenta of the escaping nucleons. Asymptotically, the potential interactions are the main origin of the overall out-of-plane elliptic flow, v_2, apart from reactions at energies below $1A$ GeV where the collisions contribute equally when the nuclear matter EoS is soft; i.e., the number of collisions is large.

The present scenario is very different from that at ultrarelativistic energies where the highly compressed overlap region develops a positive v_2 which is scaling with eccentricity of the almond shaped overlap region which is converted by the pressure gradient into a momentum asymmetry after the resulting expansion. At low energies, the internal Fermi motion of the nucleons is of the same order of magnitude as the momentum changes due to the density gradients. The passing time is long and the nucleons in the overlap region react to the sudden increase in density by expanding while projectile and target remnants are passing. The higher the beam energy the shorter is the passing time and the less the initial Fermi motion inside the projectile and the target can change the shape of the overlap region—which becomes therefore almost frozen. At lower energies, the initial Fermi motion overwhelms the less energetic fireball at the outer part of the high density region, making the final momentum distribution almost spherical, whereas the inner core remains almond shaped. This latter is not dense enough to create the pressure necessary to convert the spatial eccentricity into a positive v_2 by the consecutive expansion. The higher the beam energy the more energy is stored in the overlap region, hence the higher gets the pressure. As a consequence, with increasing the beam energy, v_2 becomes positive, as also observed experimentally.

The excitation function of the elliptic flow parameters v_2 of midrapidity protons in ^{197}Au $+$ ^{197}Au collisions at $b = 4$ fm is shown in Fig. 11: The momentum integrated distribution is shown (dashed lines) as well as the v_2 when requiring that $u_{t0} > 0.8$ (full lines). Results with a SM (black lines) and a HM (red lines) EoS vary widely above $0.4A$ GeV beam energy. We observe in addition a strong beam energy dependence of the elliptic flow signal in this regime. A maximum of the amplitude is reached at around $0.6A$ GeV. The strength of v_2 is enhanced when focusing on protons with a large transverse velocity. Comparing with experimental observations for protons having a high $u_{t0} > 0.8$ [7] at around the same impact parameter, we find a good agreement using the soft (SM) EoS (full black line in Fig. 11) in accordance with results of Ref. [19]. There, both the amplitude and the evolution of the elliptic flow with the bombarding energy are well reproduced by the model.

From this analysis we can conclude that the elliptic flow observed in the reactions around $E_{\text{kin}} \approx 1A$ GeV for protons at midrapidity ($|y_0| < 0.2$) has two origins: The collisions
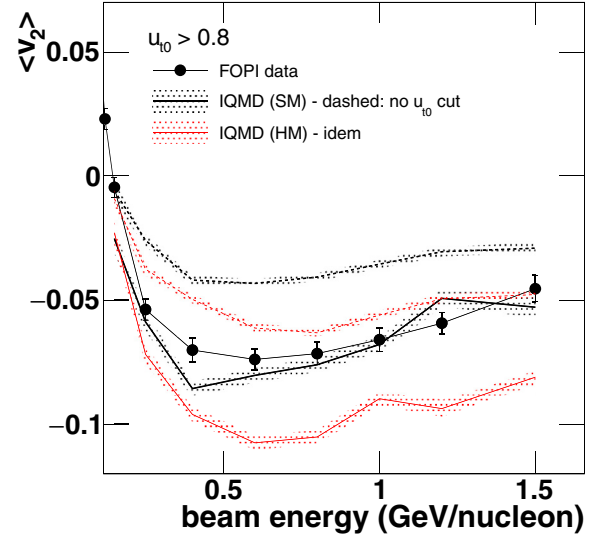

FIG. 11. Excitation function of the elliptic flow v_2 of protons at midrapidity. The experimental data (black circles) are from the FOPI collaboration published in Fig. 29 of Ref. [7]. The data is measured in the impact parameter range 3.1 fm $< b <$ 5.6 fm and a cut on $u_{t0} >$ 0.8 is applied. IQMD Model results are presented for two different nuclear EoS (HM with red lines and SM with black lines) for $b = 4$ fm and with an additional cut on $u_{t0} > 0.8$ (full lines) and without any cut (dashed lines).

of participant nucleons with the spectator matter (collisional contribution) and the acceleration of participants in the mean field (mean field contribution). The collisional component of v_2 is almost independent of the EoS, whereas the mean field contribution is for a hard EoS (HM) roughly twice as large as that for a soft EoS (SM). At lower energies ($0.6A$ GeV) for a soft EoS collisional and mean field contributions are about equal, in all other cases the contribution of the mean field dominates. The mean field induces an out-of-plane flow because those nucleons which are close to the surface of the interaction zone in y direction get accelerated out of the reaction plane due to a strong density gradient in this direction whereas nucleons close to the surface of the interaction zone in x direction see a much smaller density gradient due to the presence of the spectator matter. This effect is amplified if one selects particles with a high transverse velocity. The calculations with a soft EoS (SM) are in better agreement with the experimental data than that with a hard equation of state (HM).

V. SUMMARY

We analyzed the origin of the experimentally observed negative elliptic flow which develops at midrapidity in heavy ion reactions in the $E_{\text{kin}} \approx 1A$ GeV region. QMD calculations have shown that this elliptic flow depends stronger on the nuclear EoS than any other observable investigated so far. We have demonstrated that the EoS dependence of this negative v_2 is created by nucleons which are situated in the outer part of the overlap region of projectile and target. Between the maximum overlap and the passing time these nucleons

experience a weaker density gradient in the reaction plane as compared to out of the reaction plane, due to the presence of the spectators. This translates into a stronger force into the y direction. The density gradients and consequently the forces are stronger for a hard EoS (HM) as compared to a soft one (SM). This explains quantitatively the dependence of v_2 on the hadronic EoS. The scattering of participant protons with the spectator matter produces an elliptic flow as well, but this component is almost independent of the EoS. The agreement of the QMD calculations with data for a soft EoS adds to the circumstantial evidence that the soft EoS describes correctly the matter at a density obtained by beam energies of the order of $1A$ GeV, an observation that has already been made by analyzing the K^+ production data [20,22].

[1] H. Stöcker, L. P. Csernai, G. Graebner, G. Buchwald, H. Kruse, R. Y. Cusson, J. A. Maruhn, and W. Greiner, Phys. Rev. C **25**, 1873 (1982).

[2] G. Buchwald, G. Graebner, J. Theis, J. Maruhn, W. Greiner, H. Stöcker, K. Frankel, and M. Gyulassy, Phys. Rev. C **28**, 2349 (1983).

[3] H. Stocker and W. Greiner, Phys. Rep. **137**, 277 (1986).

[4] H. H. Gutbrod, K. H. Kampert, B. Kolb, A. M. Poskanzer, H. G. Ritter, R. Schicker, and H. R. Schmidt, Phys. Rev. C **42**, 640 (1990).

[5] M. Luzum and P. Romatschke, Phys. Rev. Lett. **103**, 262302 (2009).

[6] C. Pinkenburg *et al.* (E895 Collaboration), Phys. Rev. Lett. **83**, 1295 (1999).

[7] W. Reisdorf *et al.* (FOPI Collaboration), Nucl. Phys. A **876**, 1 (2012).

[8] A. Andronic *et al.* (FOPI Collaboration), Phys. Lett. B **612**, 173 (2005).

[9] G. Stoicea, M. Petrovici, A. Andronic, N. Herrmann, J. P. Alard, Z. Basrak, V. Barret, N. Bastid, R. Caplar, P. Crochet, P. Dupieux, M. Dzelalija, Z. Fodor, O. Hartmann, K. D. Hildenbrand, B. Hong, J. Kecskemeti, Y. J. Kim, M. Kirejczyk, M. Korolija, R. Kotte, T. Kress, A. Lebedev, Y. Leifels, X. Lopez, M. Merschmeier, W. Neubert, D. Pelte, F. Rami, W. Reisdorf, D. Schull, Z. Seres, B. Sikora, K. S. Sim, V. Simion, K. Siwek-Wilczynska, S. Smolyankin, M. Stockmeier, K. Wisniewski, D. Wohlfarth, I. Yushmanov, and A. Zhilin (FOPI Collaboration), Phys. Rev. Lett. **92**, 072303 (2004).

[10] A. Andronic, J. Lukasik, W. Reisdorf, and W. Trautmann, Eur. Phys. J. A **30**, 31 (2006).

[11] P. Danielewicz, R. Lacey, and W. G. Lynch, Science **298**, 1592 (2002).

[12] W. Reisdorf *et al.* (FOPI Collaboration), Phys. Rev. Lett. **92**, 232301 (2004).

[13] J. Y. Ollitrault, A. M. Poskanzer, and S. A. Voloshin, Phys. Rev. C **80**, 014904 (2009).

[14] L. Pang, Q. Wang, and X. N. Wang, Phys. Rev. C **86**, 024911 (2012).

[15] N. Bastid *et al.* (FOPI Collaboration), Phys. Rev. C **72**, 011901 (2005).

[16] J. Lukasik *et al.*, Phys. Lett. B **608**, 223 (2005).

[17] Y. M. Zheng, C. M. Ko, B. A. Li, and B. Zhang, Phys. Rev. Lett. **83**, 2534 (1999).

[18] P. K. Sahu, W. Cassing, U. Mosel, and A. Ohnishi, Nucl. Phys. A **672**, 376 (2000).

[19] A. Le Fèvre, Y. Leifels, W. Reisdorf, J. Aichelin, and C. Hartnack, Nucl. Phys. A **945**, 112 (2016).

[20] C. Hartnack, H. Oeschler, and J. Aichelin, Phys. Rev. Lett. **96**, 012302 (2006).

[21] J. Aichelin, Phys. Rept. **202**, 233 (1991).

[22] C. Hartnack, H. Oeschler, Y. Leifels, E. L. Bratkovskaya, and J. Aichelin, Phys. Rept. **510**, 119 (2012).

[23] C. Hartnack, R. K. Puri, J. Aichelin, J. Konopka, S. A. Bass, H. Stocker, and W. Greiner, Eur. Phys. J. A **1**, 151 (1998).

[24] S. Hama, B. C. Clark, E. D. Cooper, H. S. Sherif, and R. L. Mercer, Phys. Rev. C **41**, 2737 (1990).

[25] J. Aichelin, A. Rosenhauer, G. Peilert, H. Stocker, and W. Greiner, Phys. Rev. Lett. **58**, 1926 (1987).

[26] G. Peilert, H. Stocker, W. Greiner, A. Rosenhauer, A. Bohnet, and J. Aichelin, Phys. Rev. C **39**, 1402 (1989).

[27] C. Hartnack and J. Aichelin, Phys. Lett. B **506**, 261 (2001).